Exploring a lower resolution physics grid in CAM-SE-CSLAM

A.R. Herrington[1]*, P.H. Lauritzen[2], S. Goldhaber[2], Mark A. Taylor[3], K.A. Reed[1]

[1]School of Marine and Atmospheric Sciences, Stony Brook University, Stony Brook, New York
[2]National Center for Atmospheric Research, Boulder, Colorado, USA
[3]Sandia National Laboratories, Albuquerque, New Mexico, USA

Key Points:

-
-
-

*Stony Brook, New York

Corresponding author: Adam R. Herrington, `adam.herrington@stonybrook.edu`

Abstract

1 Introduction

Global atmospheric models fundamentally consist of two components. The dynamical core (*dynamics*), which numerically integrate the adiabatic equations of motion and tracer advection, and the physical parameterizations (*physics*), which compute the effects of diabatic and subgrid-scale processes (e.g., radiative transfer and moist convection) on the grid-scale. More out of convenience than anything else, the physics are evaluated on the dynamics grid, i.e., the physics grid and dynamics grid coincide. From linear stability and accuracy analysis of numerical methods, it is a common result that the shortest simulated wavelengths are not accurately represented by the dynamical core. Additionally, simulated downscale cascades result in an unrealistic collection of energy and/or enstrophy near the truncation scale, which may be observed from kinetic energy spectra in model simulations [*Skamarock*, 2011]. Some form of dissipation must be incorporated into models to mitigate these numerical artifacts near the grid scale [*Jablonowski and Williamson*, 2011]. This numerical dissipation has no physical analogy [although see *Grinstein et al.*, 2007], and the grid-scale is therefore contaminated by numerous un-physical processes. The under-resolved nature of the grid-scale led *Lander and Hoskins* [1997] to speculate whether the physics should be evaluated on a grid that is more reflective of the scales actually resolved by the dynamical core.

Experimentation with different physics grid resolutions have so far been limited to models employing the spectral transform method [*Lander and Hoskins*, 1997; *Williamson*, 1999; *Wedi*, 2014]. *Lander and Hoskins* [1997] argue that passing under-resolved states to the physics may be especially problematic in spectral transform models, since the physics are evaluated on a latitude-longitude transform grid, and contains more degrees of freedom than the spectral representation to prevent aliasing of quadratic quantities. However, *Lander and Hoskins* [1997] indicate that the spectral truncation of the physics tendencies damps errors that may result from passing an under-resolved state to the physics, although the extent to which these errors may still be present in the model was not addressed.

Another class of spectral-transform models evaluate the quadratic terms using semi-Lagrangian methods, which are implicitly diffusive, relaxing constraints on the resolution of the transform grid. *Wedi* [2014] experimented with different transform grid resolutions and concluded that the standard high resolution quadratic grid actually improves forecast skill over the use of a lower-resolution transform grid. They suggests that increasing the resolution of the transform grid simulates a kind of sub-grid variability on the spectral state, which is thought to be under-represented in global atmospheric models [*Shutts*, 2005]. This is in principle the purpose of "super-parameterization," in which a cloud resolving model is embedded in each grid cell to simulate the requisite subgrid variability, and improves both diurnal and sub-seasonal variability in the model [*Randall et al.*, 2003].

After the physics tendencies are transformed into spectral space, the tendencies may be truncated at any particular wave number. *Williamson* [1999] conducted a pair of convergence tests using a global spectral transform model; a conventional convergence test and one in which the spectral truncation of the physics tendencies is held fixed and the resolution of the dynamical core increased. In contrast to the realistic weather forecasts of *Wedi* [2014], *Williamson* [1999] run their model to equilibrium in an idealized climate configuration. When the physics and dynamics resolutions increase together, as in more typical convergence studies, the strength of the Hadley Cell increases monotonically with resolution. This sensitivity of Hadley Cell strength to horizontal resolution is a common result of global models at hydrostatic resolutions [see *Herrington and Reed*, 2017, and references therein]. But with the truncation wave number of physics tendencies held fixed, the Hadley Cell showed very little sensitivity to dynamical core resolution, resembling the solution for which the dynamics truncation wave number is equal to that of the lower resolution physics.

Herrington and Reed [2017] speculate that the results of *Williamson* [1999] indicate that the scales of motion resolved by the dynamical core are aliased to the lower resolution physics. It may be worth considering that if the resolution of the dynamics is reduced in response to a coarser physics grid, then the dynamics may be no better resolved on the coarser physics grid, compared with the conventional method of evaluating the physics and dynamics at the same resolution. The results of *Williamson* [1999]; *Wedi* [2014] do not provide evidence that a lower resolution physics grid reduces computational errors in spectral transform models, but this was seldom discussed in either study.

Global spectral transform models, while remarkably efficient at small processor counts, do not scale well on massively parallel systems. High-order Galerkin methods are becoming increasingly popular in climate and weather applications due to their high-parallel efficiency, high-processor efficiency, high-order accuracy (for smooth problems), and geometric flexibility facilitating mesh-refinenment applications. High resolution climate simulations with NCAR's Community Atmosphere Model [CAM; *Neale et al.*, 2012] are typically performed using a continuous Galerkin dynamical core referred to as CAM-SE [CAM Spectral Elements; *Taylor et al.*, 2008; *Dennis et al.*, 2012; *Lauritzen et al.*, 2018]. CAM-SE may be optionally coupled to a conservative, semi-Lagrangian tracer advection scheme for accelerated multi-tracer transport [CAM-SE-CSLAM; *Lauritzen et al.*, 2017]. Tracer advection then evolves on an entirely separate, finite-volume grid which contains the same degrees of freedom as CAM-SE's quadrature node grid.

Element-based Galerkin methods are susceptible to grid-imprinting, and may need be considered when contemplating a particular physics grid [*Herrington et al.*, in revision, hereafter referred to as HL18]. Grid imprinting manifests at the element boundaries, since the global basis is least smooth (C^0; all derivatives are discontinuous) for quadrature nodes lying on the element boundaries, and the gradients (e.g., the pressure gradient) are systematically tighter producing local extremes. Through computing the physics tendencies at the nodal points, element boundary extrema is also observed in the physics tendencies.

HL18 has shown that through evaluating the physics on the finite-volume tracer advection grid in CAM-SE-CSLAM, element boundary noise is substantially reduced, although still problematic in regions of steep terrain, at low latitudes. Through integrating CAM-SE's basis functions over the control volumes of the finite-volume grid, element boundary extrema is additionally weighted by the C^∞ solutions (i.e., the basis representation is infinitely smooth and all derivatives are continuous) of the element interior, and the state is smoother. Additionally, in defining an area averaged state, the finite-volume physics grid is made consistent with assumptions inherent to the physics, and is more appropriate for coupling to other model components (e.g., the land model), which is typically performed using finite-volume based mapping algorithms.

The finite-volume grid of HL18 is found through dividing the elements of CAM-SE's gnomic cubed-sphere grid with equally spaced, equi-angular coordinate lines parallel to the element boundaries, such that there are 3×3 control volumes per element (hereafter referred to as $pg3$). While a 3×3 physics grid was chosen in order to have the same degrees of freedom as the dynamical core, the control volumes encompass a region of the element in which their proximity to the element boundaries are not equal. Therefore, not every control volume in an element has the same smoothness properties. This may be avoided through defining a physics grid in which the elements are instead divided into 2×2 control volumes (hereafter referred to as $pg2$). The control volumes of the $pg2$ grid all have the same proximity to the element boundaries, and should mitigate the element boundary noise that remains in the $pg3$ grid, and shown in HL18.

In this study, we test the hypothesis that the coarser, $pg2$ physics grid is effective at reducing spurious noise at element boundaries, particularly over regions of rough topography. In addition, the recent trend towards running models at ever higher resolutions is an almost prohibitive computational burden. As the physics makes up over half of the computational cost in CAM-SE [*Lauritzen et al.*, 2018], the improvement in computational performance using a coarser resolution physics grid is potentially significant. However, any advantages of using a coarser physics grid need be weighed against any potential reduction in simulation quality, e.g., possible aliasing of the resolved scales of motion by the coarser grid, as suggested by the results of *Williamson* [1999]. Section 2 described the implementation of the $pg2$ grid into CAM-SE-CSLAM. Section 3 provides the results of a hierarchy of model configurations to identify any changes in grid imprinting, or in the overall solution, compared with the $pg3$ configuration. Section 4 provides a discussion of the results and conclusions.

2 Methods

Separating dynamics, tracer and physics grids introduces the added complexity of having to map the state from dynamics and tracer grids to the physics grid; and mapping physics tracer tendencies back to the tracer grid and physics tendencies needed by the dynamical core to the dynamics grid. The dynamics grid refers to the Gauss-Lobatto-Legendre (GLL) quadrature nodes by the spectral-element method to solve the momentum equations for the momentum vector (u, v), thermodynamics equation for temperature (T), continuity equation for dry air (M), and continuity equations for water vapor and condensates thermodynamically active [see, e.g., *Lauritzen et al.*, 2018, for details]. By tracer grid we refer to the $pg3$ grid on which CSLAM performs tracer transport of water vapor, condensates and other tracers. The GLL value for water vapor and condensates is overwritten by the CSLAM values every physics time-step so that the spectral-element advection of water species does not become decoupled from the the CSLAM advection of the same water species. Mapping velocity components, dry air mass and temperature from the GLL grid to the $pg2$ grid is done by using the internal degree 3 Lagrange basis functions in CAM-SE [as described in *Herrington et al.*, in revision, for pg3; exactly the same methods can be used for $pg2$].

As compared to the $pg3$ configuration, the extra complication of the $pg2$ setup is that tracer state needs to be mapped from the tracer grid to the physics grid and tracer tendencies need to the mapped from the physics grid to CSLAM grid. In order to describe the algorithm some notation needs to be introduced.

The mapping algorithm is applied to each element Ω (with spherical area $\Delta\Omega$) so without loss of generality consider one element. Let $\Delta A_k^{(pg)}$ and $\Delta A_\ell^{(nc)}$ be the spherical area of the physics grid grid cell $A_k^{(pg)}$ and CSLAM control volume $A_\ell^{(nc)}$, respectively. The physics grid cells and CSLAM cells respectively span the element without gaps or overlaps

$$\cup_{k=1}^{pg^2} A_k^{(pg)} = \Omega \text{ and } A_k^{(pg)} \cap A_\ell^{(pg)} = \emptyset \quad \forall k \neq \ell, \tag{1}$$

$$\cup_{k=1}^{nc^2} A_k^{(nc)} = \Omega \text{ and } A_k^{(nc)} \cap A_\ell^{(nc)} = \emptyset \quad \forall k \neq \ell. \tag{2}$$

The overlap areas between the k-th physics grid cell and CSLAM cells is denoted

$$A_{k\ell} = A_k^{(pg)} \cap A_\ell^{(nc)}, \tag{3}$$

so that

$$A_k^{(pg)} = \cup_{l=1}^{nc^2} A_{k\ell}. \tag{4}$$

This overlap grid is also referred to as an exhange grid.

2.1 Mapping tracers from CSLAM to *pg*

For mapping tracer state from the CSLAM grid to any physics grid can be done using exising CSLAM technology, i.e. do a high-order shape-preserving reconstruction of mixing ratio and dry air mass inside each CSLAM control volume and integrate those reconstruction functions over the overlap areas [*Lauritzen et al.*, 2010; *Nair and Lauritzen*, 2010]. This algorithm retains the properties of CSLAM: inherent mass-conservation, mixing ratio shape-preservation and linear-correlation preservation.

In mathemtical terms the remapping is given by

$$\Delta M_\ell^{(pg)} \Delta A_\ell = \sum_{k=1}^{nc^2} \Delta M_{k\ell}^{(nc)} \Delta A_{k\ell}, \tag{5}$$

$$\Delta M_\ell^{(pg)}\, m_\ell^{(pg)} \Delta A_\ell = \frac{1}{\Delta M_\ell^{(pg)}} \sum_{k=1}^{nc^2} \left[\Delta M\, m\right]_{k\ell}^{(nc)} \Delta A_{k\ell}, \tag{6}$$

where

$$\Delta M_{k\ell}^{(nc)} = \frac{1}{\Delta A_{k\ell}} \int_{A_{k\ell}} \Delta M(x,y) dA. \tag{7}$$

$$\left[\Delta M\, m\right]_{k\ell}^{(nc)} = \frac{1}{\Delta A_{k\ell}} \int_{A_{k\ell}} \left[\Delta M\, m\right](x,y)\, dA. \tag{8}$$

The tendencies from the parameterizations are computed on the physics grid. The tracer tendency in physics grid cell k is denoted $f_k^{(pg)}$. The problem is how to map $f_k^{(pg)}$ to the CSLAM control volumes $f^{(nc)}$ satisfying the following constraints:

1. **Local mass-conservation**

$$f_k^{(pg)} \Delta p_k^{(pg)} = \cup_{\ell=1}^{nc^2} \Delta A_{k\ell} \Delta p_\ell^{(nc)} f_\ell^{(nc)}, \tag{9}$$

   where $\Delta p_k^{(pg)}$ is the pressure level thickness in physics grid cell k and similarly for $\Delta p^{(nc)}$.
2. **Shape-preservation in mixing ratio**: The forcing on the CSLAM grid should not produce a value smaller than the new physics grid mixing ratio, $m_k^{(pg)} + \Delta t f_k^{(pg)}$ or a value smaller than the existing CSLAM mixing ratios over the overlap areas $m_{k\ell}^{(nc)}$

$$m_k^{(min)} = \min\left(m_k^{(pg)} + \Delta t f_k^{(pg)}, \left\{ m_{k\ell}^{(nc)} | \ell = 1, nc^2 \right\}\right), \tag{10}$$

   where Δt is the physics time-step. Similarly for maxima

$$m_k^{(max)} = \max\left(m_k^{(pg)} + \Delta t f_k^{(pg)}, \left\{ m_{k\ell}^{(nc)} | \ell = 1, nc^2 \right\}\right), \tag{11}$$

3. **Linear correlation preservation**: The physics forcing must not disrupt linear tracer correlation between species on the CSLAM grid [see, e.g., *Lauritzen and Thuburn*, 2012].
4. **Consistency**: A constant mixing ratio tendency, $cnst$, on the physics grid, $f_k^{(pg)} = cnst\ \forall k$, must result in the same (constant) forcing on the CSLAM grid, $f_\ell^{(nc)} = f_k^{(pg)} = cnst\ \forall \ell$.

To motivate the algorithm that will simultaneously satisfy 1-4 it is informative to discuss how 'standard' mapping algorithms will violate one or more of the constraints.

- Conservative remapping:
- Interpolation:

some text about how challenging it is to satisfy 1-3 simultaneously

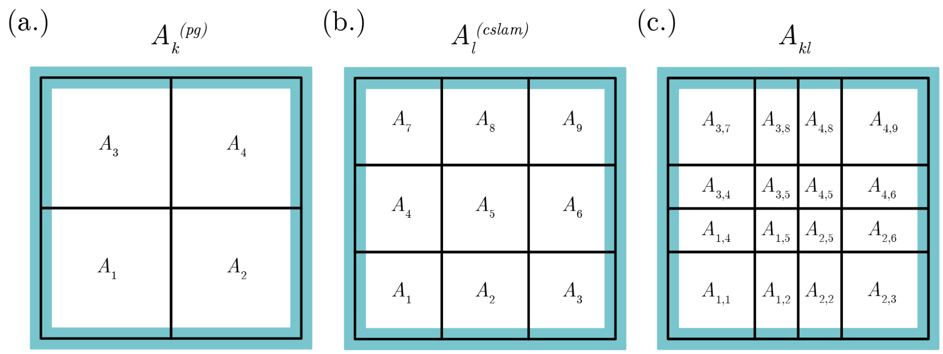

Figure 1. Indice notation for the (a) $pg2$ grid, (b), $pg3$ grid and (c) their exchange grid. Peter - do you think you will use this figure?

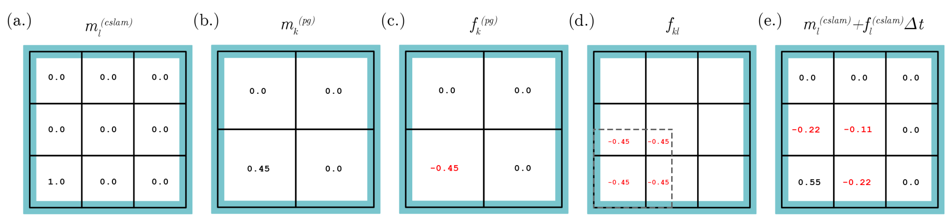

Figure 2. Make captions stand-alone while being concise

2.2 Algorithm

In the $pg2$ configuration, mapping the fields to and from the quadrature grid and $pg2$ grid is identical to that described in HL18. As discussed above above, in mapping to the physics grid, CAM-SE's Lagrange basis functions are integrated over the $pg2$ control volumes to provide the physics with a volume averaged state. The procedure is accurate to machine precision, conserves thermal energy and dry air mass, and is consistent (i.e., the mapping preserves a constant). The reverse mapping, from the physics grid to the quadrature grid, is done using a tensor-product Lagrange interpolation (see Appendix A in HL18). The Lagrange interpolation is consistent, conserves dry air mass (Peter, is this true?), but does not conserve thermal energy. Errors arising from the lack of energy conservation were estimated to be small; about two orders of magnitude less than the energy dissipation due to the dynamical core alone.

The semi-Lagrangian advection of tracers in our $pg2$ configuration is solved on the CSLAM grid. Preserving linear correlations in mapping to and from the CSLAM and $pg2$ grids requires additional considerations; one such problem is depicted schematically in Figure **??**. Consider a single element of CSLAM control volumes, containing only a single cell with mixing ratio 1.0, and 0.0 everywhere else (m_l; Figure **??**a). Assume that the mixing ratios mapped to the $pg2$ grid (m_k; Figure **??**b) result in a negative tracer tendency from the physics (f_k; Figure **??**c). The non-zero values of the tendencies for $pg2$ areas overlapping CSLAM grid cells originally containing a value of zero ($f_{k,l}$; Figure **??**d), are driven negative by the mapped tendency (Figure **??**e). Preserving linear correlations is therefore difficult since the mapping between CSLAM and $pg2$ is not reversible. Simulations performed without addressing this artifact were found to be in serious error.

Describe algorithm here

Peter - I think the results of the terminator tests should be mentioned here. We could just put in a sentence saying it passes. But I'm assuming that if we don't use the algorithm that weights the tendency by the amount of available mixing ratio, it will fail. If that's the case, we could just do a two panel plot showing the iCLy at day 15 for with and without the algorithm.

2.2.1 Model Configurations

Two model configurations using CESM2.1 (`https://doi.org/10.5065/D67H1H0V`) are chosen to carry out the objectives discussed in Section 1. To test the hypothesis, that the $pg2$ grid reduces spurious grid-noise over mountainous regions, a Held-Suarez configuration [$FHS94$ compset; *Held and Suarez*, 1994] modified to include real world topography is analyzed. HL18 indicate that this configuration tends to have more grid-noise over steep terrain than in a more complex configuration using CAM, version 6 moist physics [CAM6;], and is therefore a conservative choice for evaluating any change in grid imprinting between $pg3$ and $pg2$.

To understand whether the resolved scales of motion are influenced by the use of a coarser resolution physics grid, a suite of aqua-planet simulations [*Neale and Hoskins*, 2000; *Medeiros et al.*, 2016] are carried out over a range of spectral-element grid resolutions, using CAM6 physics ($QPC6$ compset). An aqua-planet is an ocean covered planet in perpetual equinox, with fixed, zonally-symmetric sea surface temperatures idealized after present day Earth. In CAM, their is a strong sensitivity of solutions to the physics time-step [Δt_{phys}; *Williamson and Olson*, 2003; *Williamson*, 2013; *Herrington and Reed*, 2018] and it is unclear how Δt_{phys} should vary across resolutions.

Here, a scaling for Δt_{phys} across resolutions is proposed, based on results of the moist bubble test [*Herrington and Reed*, 2018] using CAM-SE-CSLAM and detailed in the Appendix. The scaling is linear in Δx_{dyn} and analogous to a CFL criterion,

$$\Delta t_{phys} = \Delta t_{phys,0} \times \Delta x_{dyn} / \Delta x_{dyn,0} \ , \tag{12}$$

where $\Delta t_{phys,0}$ is taken to be the standard $1800s$ used in CAM-SE-CSLAM at low resolution, $\Delta x_{dyn,0} = 111.2km$.

2.3 Model Configurations

3 Results

3.1 Held-Suarez with Topography

Flow over rough topography can result in significant grid imprinting using the spectral element method [*Lauritzen et al.*, 2015; *Herrington et al.*, in revision]. Figure 2 shows the results of the Held-Suarez with topography simulations. The middle panel is the vertical pressure velocity, ω, averaged over two years, over the Andes and Himalayan region at two different levels in the mid-troposphere, using the $ne30pg3$ grid. The fields are displayed as a raster plot on the physics grid, so that individual extrema, which characterize the flow over the Andes between about $10° - 20°$ S, and the Himalayas between $20° - 30°$ N, may be identified as spurious.

As discussed in *Herrington et al.* [in revision], grid imprinting over mountainous terrain tend to occur in regions of weak gravitational stability, causing extrema to extend through the full depth of the troposphere as resolved updrafts and downdrafts. Thus, grid imprinting over mountains may be alleviated through increasing the divergence damping

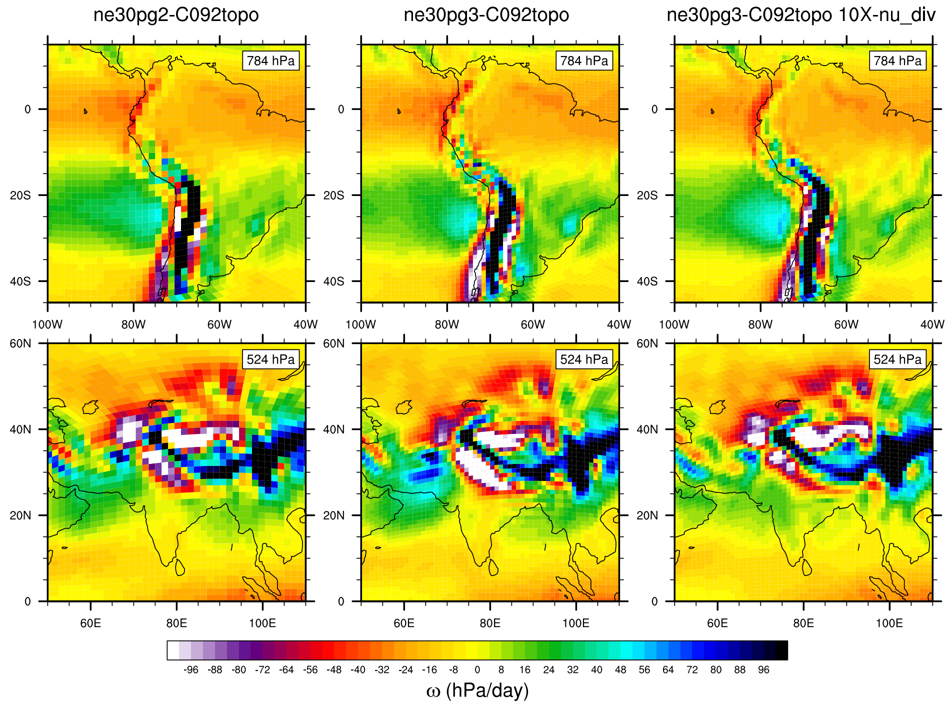

Figure 3. Mean ω at two model levels in the middle troposphere, in a Held-Suarez configuration outfitted with real world topography. (Left) $ne30pg2$ (Middle) $ne30pg3$ and (Right) $ne30pg3$ with the divergence damping coefficient increased by an order of magnitude. The ω fields are computed a two-year simulation. The data are presented on a raster plot in order to identify individual grid cells

in the model. The spectral element method is not implicitly dissipative, so fourth-order hyperviscosity operators are applied to the prognostic variables [*Lauritzen et al.*, 2018]. Figure 2 (right panel) repeats the $ne30pg3$ simulation through increasing the hyperviscous divergence damping coefficient by an order of magnitude. The spurious noise over the Andes and the Himalayas are damped, and grid point extrema tend to diffuse into neighboring grid cells. The wavenumber-power spectrum of the kinetic energy arising from divergent modes is provided in Figure 3, confirming that divergent modes are significantly damped at higher wavenumbers relative to the default $ne30pg3$ simulation.

The ω field in a $ne30pg2$ simulation is provided in Figure 2 (left panel). Grid cell extrema over the Andes is less prevalent than in the $ne30pg3$ simulation, as seen by the reduction in large magnitude ω (e.g., red grid cells). The spurious oscillations at the foot of the Himalayas appear to have been entirely eliminated. This improvement in grid imprinting is due to the consistent numerical properties of the control volumes in the $pg2$ configuration discussed in Section 1. The divergent modes are slightly damped relative to the $ne30pg3$ simulations only at large wavenumbers (greater than 50), and much less damped compared to the simulation with large divergence damping (Figure 3).

3.2 Aqua-planets

When the physics and dynamics grids are of a different resolution, it is not clear which grid determines the resolved scales of motion. This may be tested through comparing $ne30pg2$, which has a physics grid spacing of approximately $166.8km$, to a $ne20pg3$ simulation, in which the physics and the dynamics both have an approximate grid spac-

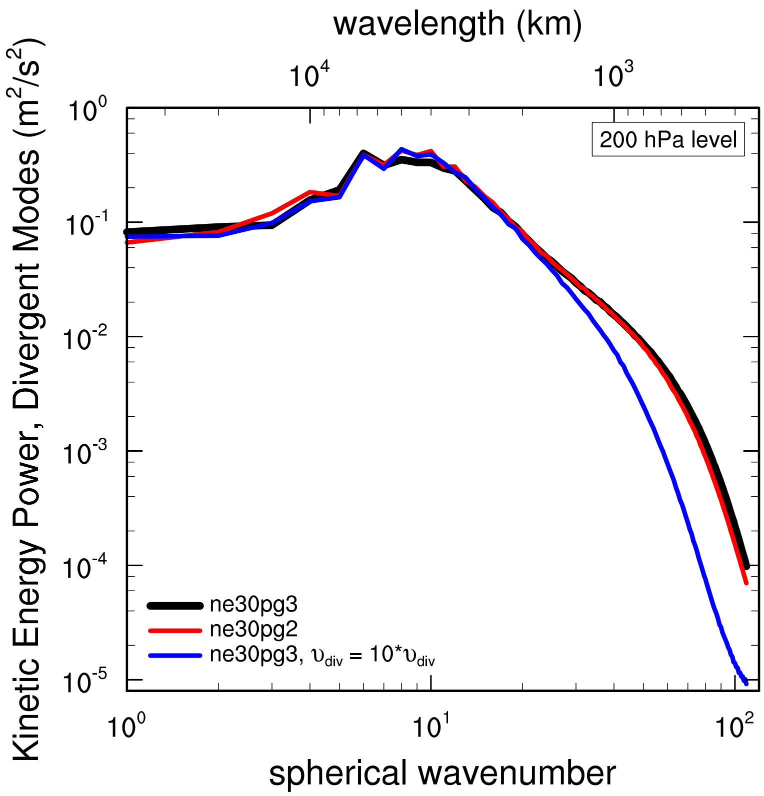

Figure 4. Kinetic energy power spectrum arising from divergent modes in $ne30pg3$, $ne30pg2$ and $ne30pg3$ with the divergence damping coefficient increased by an order of magnitude, in the Held-Suarez with topography simulations. Spectra computed from five months of six-hourly winds.

ing of $166.8km$. Further, these two solutions are compared against an $ne30pg3$ simulation, which acts as an upper bound on the $ne30pg2$ solution; the $ne20pg3$ solution then being a lower bound (see Table 1). The probability density function (PDF) of upward ω everywhere in the simulations is shown in Figure 4b. While in practice the model state is defined to be the physics grid, ω here is shown on the GLL grid. It is clear that larger magnitude ω is more frequent in $ne30pg2$, as compared with $ne20pg3$, and is actually more similar to the $ne30pg3$ distribution.

Figure 4a shows the wave-number power spectrum of the forcing on the GLL grid in the middle-to-upper troposphere, where stratiform heating is common due to detrainment of moisture by the deep convections scheme [*Zhang and McFarlane*, 1995]. The variance is larger for higher wavenumbers in $ne30pg3$ and $ne30pg2$, as compared with $ne20pg3$, supporting the notion that buoyancy length scales (hereafter referred to as D) are larger in $ne20pg3$. The larger D in $ne20pg3$ is consistent with the scale analysis in that the frequency of large magnitude ω is lower, compared with the $ne30pg2$ and $ne30pg3$ simulations.

The $ne30pg2$ spectra is remarkably similar to the $ne30pg3$ spectra (Figure 4a), consistent with their similar distribution of large magnitude ω in Figure 4b. These figures suggest that D is very similar in $ne30pg2$ and $ne30pg3$. This is further illustrated through scaling the PDF's,

$$P(\omega_s) = \alpha \times P(\omega/\alpha), \tag{13}$$

where $P(\omega_s)$ is the PDF of the scaled ω, ω_s, and α is the ratio of the ω to ω of the target grid resolution. Using equation A.1, and assuming that D is linearly related to the grid-spacing [and that the parcel buoyancy and the characteristic vertical scale of buoyancy is unchanged or compensating *Jeevanjee and Romps*, 2016], $\alpha = \Delta x_{target}/\Delta x$, where Δx_{target} is the grid spacing of the target resolution, taken here to be the grid spacing of the $ne30pg3$ grid.

If D is in fact determined by the physics grid spacing, Δx_{phys}, then one sets $\Delta x = \Delta x_{phys}$ in α for the $ne30pg2$ simulation. This scaled PDF, however, severly overestimates the frequency of upward ω of the target resolution, $ne30pg3$ (Figure 4c). It is clear from the similarity of the un-scaled PDF's that D is determined by the dynamics grid spacing, Δx_{dyn}. The scaled $ne20pg3$ PDF agree's quite well with the $ne30pg3$ distribution, suggesting that the scale parameter α explains the difference in vertical motion between the two simulations.

The authors have determined that there are two reasons D is determined by the dynamics grid, and not the physics grid, in $ne30pg2$. The first reason, is that the hyperviscosity coefficients are a function of Δx_{dyn}, and therefore the same in the $pg2$ and $pg3$ simulations. The fourth-order hyperviscosity is rather scale selective, targeting near grid-scale features more so than a second-order operator. The difference in Δx_{phys} between $pg2$ and $pg3$ are small enough that the hyperviscosity renders this distinction somewhat ambiguous ($pg2$ is a factor 1.5 larger than $pg3$). The second reason D is determined by Δx_{dyn}, is that high-order mapping of the physics tendencies from $pg2$ to the higher-resolution GLL and $CSLAM$ grids helps to reconstruct scales that are not present on the $pg2$ grid.

The left panel of Figure 5a shows a close-up of the wavenumber power spectrum of the forcing on the physics grid (dotted) and the GLL grid (solid). In $ne30pg3$, the variances are similar, and even damped at higher wavenumbers (larger than 65) on the GLL grid compared to the physics grid. Through using high-order mapping in $ne30pg2$, the variance on the GLL grid is actually larger than on the $pg2$ grid, matching the variance of the $ne30pg3$ forcing on the GLL grid, mentioned earlier in reference to Figure 4a. Since the adiabatic dynamics is prognosed on the GLL grid, the similar forcing variance on the GLL grid in $ne30pg2$ and $ne30pg3$ is consistent with the similar PDFs of ω on the GLL grid in the two simulations (see Figure 5, right panel). Repeating the $ne30pg2$ simulation, but using low-order mapping, i.e., piecewise constant mapping from $pg2$ to $CSLAM$ and bilinear mapping from $pg2$ to GLL, the forcing variance on the GLL grid is similar, and even slightly less at high wavenumbers than on the $pg2$ grid. Following suit, the frequency of large magnitude ω on the GLL grid in the low-order run is less compared to the default $ne30pg2$ simulation (Figure 5, right panel).

Through using the low-order mapping in $ne30pg2$, and by increasing the hyperviscosity coefficients to match the $ne20pg3$ simulation, the simulation more closely resembles the $ne20pg3$ run (Figure 4). In this case, D is more accurately determined by Δx_{phys}, since the scaled PDF matches the $ne30pg3$ simulation quite well. Therefore, at low resolution, our default $ne30pg2$ configuration does not indicate that the scales of motion are aliased to resolution of the coarser resolution physics grid, as they more closely resemble the $ne30pg3$ solution.

3.2.1 High Resolution

The physics time-step, Δt_{phys}, used for each grid is scaled by the dynamics time-step to prevent time truncation errors at higher resolutions [*Herrington and Reed*, 2018].

Table 1. Average equatorial grid spacing, Δx, and model time-step, Δx, used by the physical parameterizations, $phys$, and dynamical core, dyn.

Grid name	Δx_{dyn}	Δt_{dyn}	Δx_{phys}	Δt_{phys}
ne20pg3	166.8km	300s	166.8km	1800s
ne30pg2	111.2km	300s	166.8km	1800s
ne30pg3	111.2km	300s	111.2km	1800s

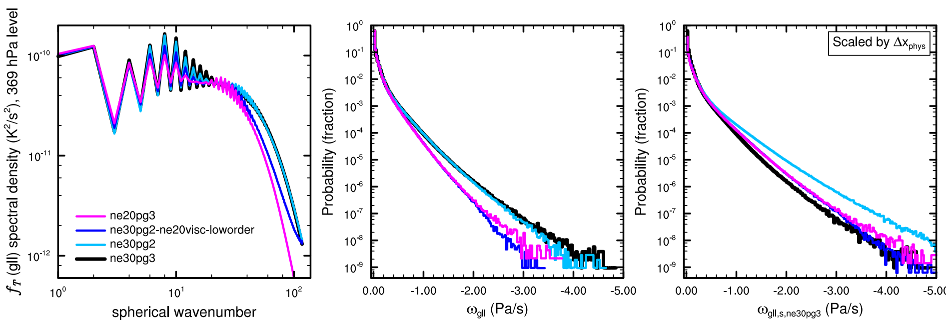

Figure 5. (Left) Wavenumber-power spectrum of the temperature tendencies from the moist physics, near the 369 hPa level, (Middle) probability density distribution and (Right) the scaled probability density distribution of upward ω everywhere in the model. The scaled distributions are scaled to $ne30pg3$ using Δx_{phys}.

3.2.2 Across Resolutions

4 Conclusions

Mitigating grid-imprinting through increasing the divergence damping coefficient an order of magnitude greater than is required for numerical stability is not ideal from a model development perspective. The hyper-viscosity coefficients are one of the only a handful of free-parameters in CAM-SE to tune the kinetic energy spectrum to match observations [*Skamarock et al.*, 2014; *Lauritzen et al.*, 2018].

A: Defining Δt_{phys} across resolutions

Herrington and Reed [2018] developed a moist bubble test, which indicate that time-truncation errors are large at high resolution (roughly 50km and less), and may provide incite on a reasonable scaling of Δt_{phys} across resolutions in more complex configurations. In the moist bubble test a set of non-rotating simulations are performed, in which the grid spacing and bubble radius are simultaneously reduced by the same factor in each run through varying the planetary radius. The test was designed to mimic the reduction in buoyancy length scales that occur when the model resolution is increased in more complex configurations [*Hack et al.*, 2006; *Herrington and Reed*, 2018].

The moist bubble test is performed with CAM-SE-CSLAM and coupled to the simple condensation routine of *Kessler* [1969] across five different resolutions ($ne30$, $ne40$, $ne60$, $ne80$, and $ne120$). The results are expressed as the minimum ω throughout each one day simulation, and shown in Figure A.1. Two sets of simulations are performed with both $pg3$ and $pg2$, one with Δt_{phys} determined by equation 12, and an equivalent set of simulations with $\Delta t_{phys} = \Delta t_{phys,0}$ for all resolutions.

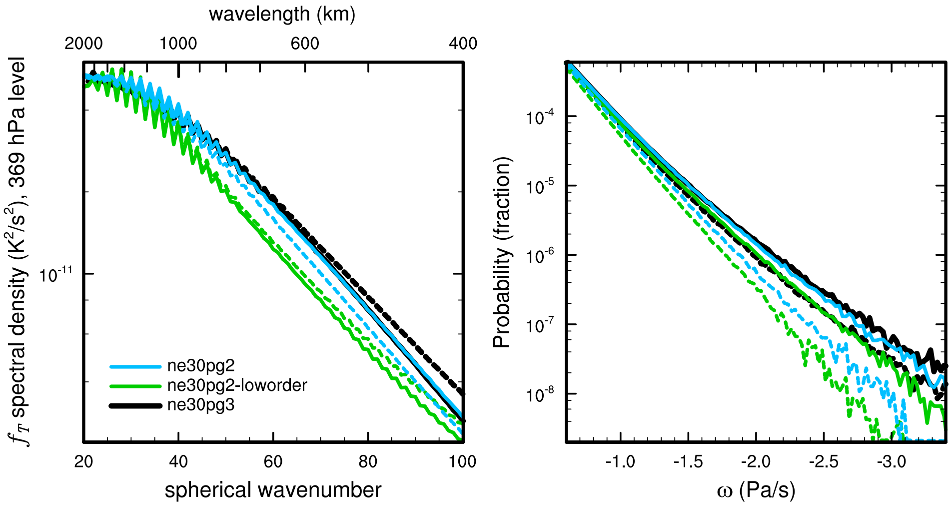

Figure 6. (Left) Wavenumber-power spectrum of the temperature tendencies from the moist physics, near the 369 hPa level, and (right) probability density distribution of upward ω, everywhere in the model, for three year-long aqua-planet simulations. Solid lines refer to values of on the dynamics grid, and dashed lines, the values on the physics grid. See text for details regarding the three simulations.

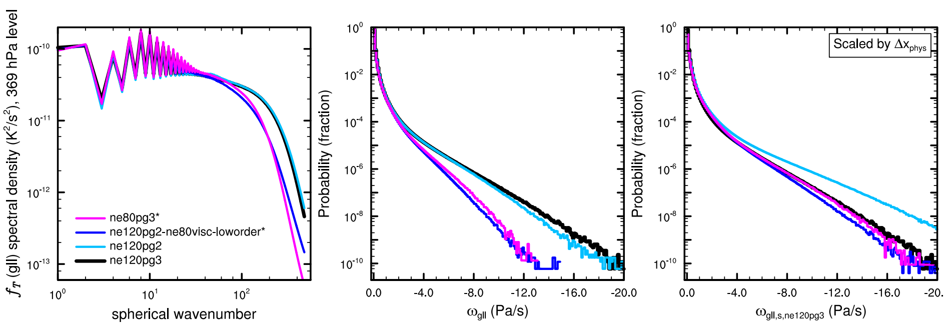

Figure 7. As in Figure 4, but for the high resolution simulations. Asterisks indicate that the physics time-step in these simulations are $\Delta t_{phys} = 675s$, which is larger than those used in the default $ne120$ grid of $\Delta t_{phys} = 450s$ (see Table **??**).

Herrington and Reed [2018] has shown that ω converges to the scaling of,

$$\omega = \omega_0 \times \Delta x_{dyn,0} / \Delta x_{dyn} \ , \tag{A.1}$$

in the limit of small Δt_{phys} (small Δt_{phys} is defined here as $\Delta t_{phys} = \Delta t_{dyn}$, where Δt_{dyn} is the CFL limiting time-step). Equation A.1 is plotted as grey lines in Figure A.1, derived from a scale analysis of the Poisson equation [*Jeevanjee and Romps*, 2016] at hydrostatic scales. The solutions using Δt_{phys} from equation 12 follow the scaling, whereas fixing $\Delta t_{phys} = 1800s$ across resolutions damps the solution relative to the analytical solution, progressively more so at higher resolutions. The magnitude of ω in the $pg3$ solutions are systematically larger than the $pg2$ solutions, which is primarily a result of the damping effect of integrating the basis functions over a larger control volume.

It should be noted that equation A.1 is only strictly valid for the dry anelastic equations, and that the scaling is maintained when including moist processes is not proven

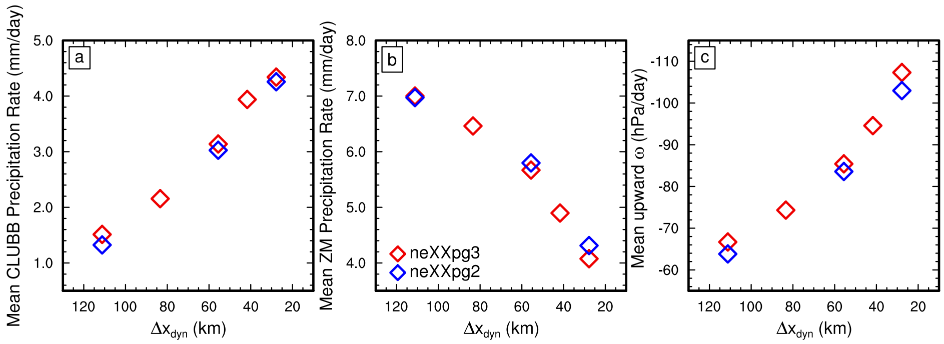

Figure 8. Year long mean values, averaged over +/-10° latitude.

through theory. Regardless, if Δt_{phys} is too large, the solution has non-negligible error, which is avoided through scaling Δt_{phys} using equation 12.

The results of the idealized test may not extend to the results of more complex configurations. To get a a handle on whether the test is useful for understanding more realistic configurations, four aqua-planet simulations are performed with CAM6 physics. A pair of $ne30pg2$ simulations, one in which Δt_{phys} is determined by the scaling of equation A.1, and one where it is set to the Δt_{phys} appropriate for the $ne20$ resolution. Figure A.2a shows a pair of PDFs of ω, computed from one year of 6-hourly data of the entire model domain. The curves are barely discernible from one another, and indicate that at lower resolution, the solutions are not that sensitive to Δt_{phys}. Figure A.2b shows the PDFs of a pair of $ne120pg2$ simulations, similarly, with Δt_{phys} determined by equation A.1, and one with Δt_{phys} set to the $ne80$ value. Large values of ω (less then $1Pa/s$) are much more frequent in the smaller Δt_{phys} simulation.

The results in Figure A.2 are similar to the CAM, version 5 aqua-planet results of *Herrington and Reed* [2018], showing that solutions are more sensitive to Δt_{phys} at higher-resolutions. This behavior also manifests in the moist bubble tests, indicating that the time-truncation errors arising from large Δt_{phys} also exist in more complex configurations.

References

Dennis, J. M., J. Edwards, K. J. Evans, O. Guba, P. H. Lauritzen, A. A. Mirin, A. St-Cyr, M. A. Taylor, and P. H. Worley (2012), CAM-SE: A scalable spectral element dynamical core for the Community Atmosphere Model, *Int. J. High. Perform. C.*, *26*(1), 74–89, doi:10.1177/1094342011428142.

Grinstein, F. F., L. G. Margolin, and W. J. Rider (Eds.) (2007), *Implicit Large Eddy Simulation: Computing turbulent fluid dynamics*, Cambridge University Press.

Hack, J., M. Caron, G. Danabasoglu, K. W. Oleson, C. Bitz, and J. Truesdale (2006), Ccsm–cam3 climate simulation sensitivity to changes in horizontal resolution, *19*(1), 2269–2289.

Held, I. M., and M. J. Suarez (1994), A proposal for the intercomparison of the dynamical cores of atmospheric general circulation models, *Bull. Am. Meteorol. Soc.*, *73*, 1825–1830.

Herrington, A., and K. Reed (2018), An idealized test of the response of the community atmosphere model to near-grid-scale forcing across hydrostatic resolutions, *J. Adv. Model. Earth Syst.*, *10*(2), 560–575.

Herrington, A., P. Lauritzen, M. A. Taylor, S. Goldhaber, B. E. Eaton, J. Bacmeister, K. Reed, and P. Ullrich (in revision), Physics-dynamics coupling with element-based

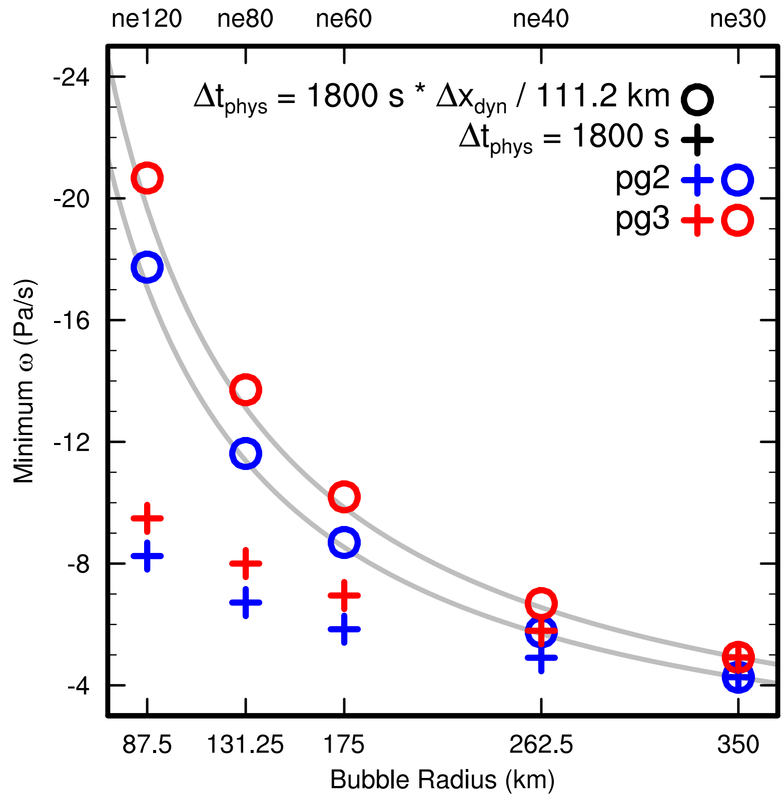

Figure A.1.

high-order galerkin methods: quasi equal-area physics grid, *Mon. Wea. Rev.*

Herrington, A. R., and K. A. Reed (2017), An explanation for the sensitivity of the mean state of the community atmosphere model to horizontal resolution on aquaplanets, *J. Climate*, *30*(13), 4781–4797, doi:10.1175/jcli-d-16-0069.1.

Jablonowski, C., and D. L. Williamson (2011), The pros and cons of diffusion, filters and fixers in atmospheric general circulation models., in: P.H. Lauritzen, R.D. Nair, C. Jablonowski, M. Taylor (Eds.), Numerical techniques for global atmospheric models, *Lecture Notes in Computational Science and Engineering, Springer, 2010, in press.*, *80*.

Jeevanjee, N., and D. M. Romps (2016), Effective buoyancy at the surface and aloft, *Quart. J. Roy. Meteor. Soc.*, *142*(695), 811–820.

Kessler, E. (1969), On the distribution and continuity of water substance in atmospheric circulations, *Meteorol. Monogr.*, *10*(32), 88.

Lander, J., and B. Hoskins (1997), Believable scales and parameterizations in a spectral transform model, *Mon. Wea. Rev.*, *125*, 292–303., doi:10.1175/1520-0493.

Lauritzen, P., and J. Thuburn (2012), Evaluating advection/transport schemes using interrelated tracers, scatter plots and numerical mixing diagnostics, *Quart. J. Roy. Met. Soc.*, *138*(665), 906–918, doi:10.1002/qj.986.

Lauritzen, P. H., R. D. Nair, and P. A. Ullrich (2010), A conservative semi-Lagrangian multi-tracer transport scheme (CSLAM) on the cubed-sphere grid, *J. Comput. Phys.*, *229*, 1401–1424, doi:10.1016/j.jcp.2009.10.036.

Lauritzen, P. H., J. T. Bacmeister, P. F. Callaghan, and M. A. Taylor (2015), Ncar global model topography generation software for unstructured grids, *Geoscientific Model Development Discussions*, *8*(6), 4623–4651, doi:10.5194/gmdd-8-4623-2015.

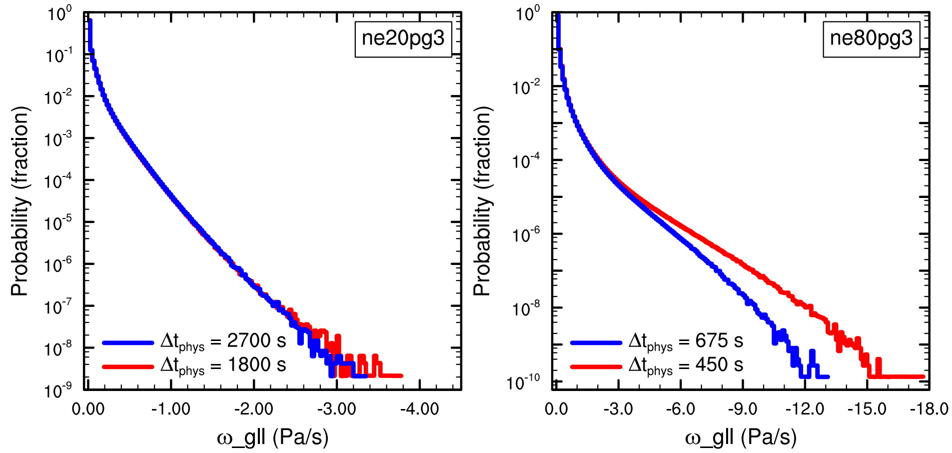

Figure A.2. Probability density distribution of upward ω everywhere in the model in the aqua-planets for the $ne20pg3$ grid (Left) and the $ne80pg3$ grid (Right). Figure computed for one year of 6-hourly data. The different colors indicate the physics time-steps used in the runs.

Lauritzen, P. H., M. A. Taylor, J. Overfelt, P. A. Ullrich, R. D. Nair, S. Goldhaber, and R. Kelly (2017), CAM-SE-CSLAM: Consistent coupling of a conservative semi-lagrangian finite-volume method with spectral element dynamics, *Mon. Wea. Rev.*, *145*(3), 833–855, doi:10.1175/MWR-D-16-0258.1.

Lauritzen, P. H., R. Nair, A. Herrington, P. Callaghan, S. Goldhaber, J. Dennis, J. T. Bacmeister, B. Eaton, C. Zarzycki, M. A. Taylor, A. Gettelman, R. Neale, B. Dobbins, K. Reed, and T. Dubos (2018), NCAR CESM2.0 release of CAM-SE: A reformulation of the spectral-element dynamical core in dry-mass vertical coordinates with comprehensive treatment of condensates and energy, *J. Adv. Model. Earth Syst.*, doi:10.1029/2017MS001257.

Medeiros, B., D. L. Williamson, and J. G. Olson (2016), Reference aquaplanet climate in the community atmosphere model, version 5, *J. Adv. Model. Earth Syst.*, *8*(1), 406–424, doi:10.1002/2015MS000593.

Nair, R. D., and P. H. Lauritzen (2010), A class of deformational flow test cases for linear transport problems on the sphere, *J. Comput. Phys.*, *229*, 8868–8887, doi:10.1016/j.jcp.2010.08.014.

Neale, R. B., and B. J. Hoskins (2000), A standard test for agcms including their physical parametrizations: I: the proposal, *Atmos. Sci. Lett*, *1*(2), 101–107, doi:10.1006/asle.2000.0022.

Neale, R. B., C.-C. Chen, A. Gettelman, P. H. Lauritzen, S. Park, D. L. Williamson, A. J. Conley, R. Garcia, D. Kinnison, J.-F. Lamarque, D. Marsh, M. Mills, A. K. Smith, S. Tilmes, F. Vitt, P. Cameron-Smith, W. D. Collins, M. J. Iacono, R. C. Easter, S. J. Ghan, X. Liu, P. J. Rasch, and M. A. Taylor (2012), Description of the NCAR Community Atmosphere Model (CAM 5.0), *NCAR Technical Note NCAR/TN-486+STR*, National Center of Atmospheric Research.

Randall, D., M. Khairoutdinov, A. Arakawa, and W. Grabowski (2003), Breaking the cloud parameterization deadlock, *Bulletin of the American Meteorological Society*, *84*(11), 1547–1564.

Shutts, G. (2005), A kinetic energy backscatter algorithm for use in ensemble prediction systems, *Quart. J. Roy. Meteorol. Soc.*, *131*, 3079–3102.

Skamarock, W. (2011), Kinetic energy spectra and model filters, in: P.H. Lauritzen, R.D. Nair, C. Jablonowski, M. Taylor (Eds.), Numerical techniques for global atmospheric models, *Lecture Notes in Computational Science and Engineering, Springer*, *80*.

Skamarock, W. C., S.-H. Park, J. B. Klemp, and C. Snyder (2014), Atmospheric kinetic energy spectra from global high-resolution nonhydrostatic simulations, *Journal of the Atmospheric Sciences*, *71*(11), 4369–4381, doi:10.1175/JAS-D-14-0114.1.

Taylor, M., J. Edwards, and A. St-Cyr (2008), Petascale atmospheric models for the community climate system model: new developments and evaluation of scalable dynamical cores, *J. Phys.: Conf. Ser.*, *125*, doi:10.1088/1742-6596/125/1/012023.

Wedi, N. P. (2014), Increasing horizontal resolution in numerical weather prediction and climate simulations: illusion or panacea?, *Philosophical Transactions of the Royal Society of London A: Mathematical, Physical and Engineering Sciences*, *372*(2018), doi: 10.1098/rsta.2013.0289.

Williamson, D. L. (1999), Convergence of atmospheric simulations with increasing horizontal resolution and fixed forcing scales, *Tellus A*, *51*, 663–673, doi:10.1034/j.1600-0870.1999.00009.x.

Williamson, D. L. (2013), The effect of time steps and time-scales on parametrization suites, *Quart. J. Roy. Meteor. Soc.*, *139*(671), 548–560, doi:10.1002/qj.1992.

Williamson, D. L., and J. G. Olson (2003), Dependence of aqua-planet simulations on time step, *Q. J. R. Meteorol. Soc.*, *129*(591), 2049–2064.

Zhang, G., and N. McFarlane (1995), Sensitivity of climate simulations to the parameterization of cumulus convection in the canadian climate center general-circulation model, *ATMOSPHERE-OCEAN*, *33*(3), 407–446.